inorganics

MDPI

Article

Wide-Bandgap A_2TiSiO_6 (A = Ca, Sr, Ba) Double Perovskites for Optoelectronic Applications

Łukasz Szeleszczuk [1,*], Katarzyna Mądra-Gackowska [2] and Marcin Gackowski [3]

[1] Department of Organic and Physical Chemistry, Medical University of Warsaw, 1 Banacha Str., 02-097 Warsaw, Poland
[2] Department of Geriatrics, L. Rydygier Collegium Medicum in Bydgoszcz, Nicolaus Copernicus University in Torun, 9 Skłodowskiej Curie Str., 85-094 Bydgoszcz, Poland; katarzyna.madra@cm.umk.pl
[3] Department of Toxicology and Bromatology, L. Rydygier Collegium Medicum in Bydgoszcz, Nicolaus Copernicus University in Torun, 2 Jurasza Str., 85-089 Bydgoszcz, Poland; marcin.gackowski@cm.umk.pl
* Correspondence: lukasz.szeleszczuk@wum.edu.pl; Tel.: +48-501-255-121

Abstract

The structural, mechanical, electronic, and optical properties of cubic double perovskite oxides A_2TiSiO_6 (A = Ca, Sr, Ba) were systematically investigated using first-principles density functional theory calculations. Structural optimization within the GGA–PBE framework confirms that all compounds crystallize in a stable cubic phase. The negative formation energies indicate thermodynamic stability and potential experimental synthesizability. Ab initio molecular dynamics (AIMD) simulations performed at 300 K further confirm the dynamical stability of all compounds under finite-temperature conditions. The Born–Huang stability criteria performed elastic constant analysis establishes mechanical stability and the derived mechanical moduli indicate the presence of rigid but brittle behavior with moderate amounts of elastic anisotropy. Calculation of the electronic band structure reveals that all the compounds are direct wide-bandgap semiconductors, with the HSE06 bandgaps of Ca_2TiSiO_6, Sr_2TiSiO_6 as well as Ba_2TiSiO_6 being 2.61, 2.50 and 2.37 eV, respectively. The optical property analysis has shown that they are strong in terms of their absorption in the visible–ultraviolet region, with high dielectric constants and good refractive indices, which makes them appropriate in optoelectronics and photovoltaic applications. On the whole, A_2TiSiO_6 double perovskites are promising for use as wide-bandgap materials in the development of superior optoelectronic devices.

Keywords: DFT; thermodynamic stability; elastic properties; direct bandgap; optical properties

Check for updates

Academic Editor: Pengfei Wu

Received: 3 April 2026
Revised: 5 May 2026
Accepted: 7 May 2026
Published: 8 May 2026

Copyright: © 2026 by the authors. Licensee MDPI, Basel, Switzerland. This article is an open access article distributed under the terms and conditions of the Creative Commons Attribution (CC BY) license.

1. Introduction

Double perovskite oxides (DPOs) represent an important and highly versatile class of materials, distinguished by their remarkable chemical flexibility and the vast range of possible compositions and structures. These materials typically crystallize in the $A_2BB'O_6$ structure, where A denotes a rare-earth or alkaline-earth metal, B and B′ are transition-metal cations, and O represents oxygen. Owing to this flexible composition, DPOs exhibit a wide variety of unusual and technologically valuable chemical and physical properties [1–3]. These include diverse electronic behaviors such as insulating and metallic states [4], half-metallic spin-polarized conductivity [5], superconductivity, and strong magnetoresistance effects [6–8]. Moreover, DPOs exhibit ionic conductivity, catalytic behavior, ferroelectric and piezoelectric behavior as well as serves as an electrolyte material in fuel cells [9]. In

addition, the operation and improvement of the solar cells depend greatly on the use of the double perovskite oxides [10,11]. DPO materials have attracted much experimental and theoretical attention in the last several years due to their exceptional properties and their technological perspectives [12–14].

The attention of double perovskite oxides has been focused because they exhibit significant magnetoresistance and half-metallic properties, and they are also deemed as significant substances in solar cells and optoelectronic devices [15–18]. The twenty-first century has seen the intensive search of half-metallic (HM) materials that are attractive to spintronic devices, the electron spin degree of freedom which is used to process information and store data. Other material systems have also recently been reported to have half-metallicity, including Heusler alloys [19–21]. A high polarization level, i.e., half-metals with 100 percent spin polarization, is essential in the development of high-performance spin-based devices. The new HM materials, in particular, the double perovskite oxides are of interest as they offer structural as well as compositional flexibility, high spin polarization, and sustained ferromagnetism, often even beyond room temperature [22].

In the last ten years, a wide range of DPOs with divalent alkaline-earth cations (Sr, Ca, and Ba) at the A site, with 3d and 4d/5d transition-metal ions at the B and B sites, have been characterized computationally by density functional theory (DFT) [23–25]. In more recent publications, a number of Ba-based DPOs have been given a significant amount of attention due to their half-metallic character and stability in the cubic form [26,27]. The overall structure of such oxides with transition metals may be expressed as Z_2XMO_6 with Z being an alkaline-earth element, and X and M being the octahedral site elements. The structural, electronic, magnetic, and optical properties can be tailored by substitution of the Z, X, and M sites with alkaline-earth, transition-metal, or other metallic cations. Therefore, one of the key aims of the existing studies is to examine the connection between cation replacement and the resulting structural, electronic, elastic, magnetic, and optical properties of the Z_2XMO_6 compounds.

Of the TMDP oxides, tantalum (Ta)-based materials have been studied extensively experimentally and theoretically, such as Sr_2XTaO_6 (X = Cr, Mn) [28,29], Ba_2ScTaO_6 [30] A_2CrTaO_6 (A: Sr, Ca) [31], Ba_2InTaO_6 [32], A_2SmTaO_6 (A = Ba, Sr, Ca) [33], Ba_2YTaO_6 [34], Ba_2MTaO_6 (M = Cr, Mn, Fe) [35]. In recent years, optoelectronic and magnetic applications have also received a lot of attention in DPOs on the basis of their structural stability and elevated Curie temperature. Theoretically, low-temperature ferromagnetism has been observed in Dy_2NiMnO_6, La_2NiMnO_6 and Lu_2NiMnO_6 DPOs with bandgap values ranging from 1.2 to 1.6 eV [36–39]. Re-based double perovskites like X_2FeReO_6 (X = Ba, Sr, Ca) have also been reported to show ferromagnetic behavior useful in spintronic applications, with the 5d electrons of Re also providing intrinsic magnetic moments [40,41]. Silicate-based perovskites, where silicon (Si) is the center of interest, in particular, are receiving increasing attention due to their tunable physical characteristics, phase transitions triggered by pressure, and their possible technological uses [14]. The cubic quaternary double perovskite Ca_2TiSiO_6 is of special interest in this category. It crystallizes in cubic $Fm\bar{3}m$ space group (No. 225), with Ti and Si fully ordered in alternating octahedral positions, Ca distorted cubo-octahedral coordinated. Leinenweber, Kurt and Parise experimentally optimized the crystal structure of Ca_2TiSiO_6 and reported a lattice constant of a = 7.4105 Å [42]. Also, Husain et al. [43] conducted a theoretical study on the physical properties of the Ca_2TiSiO_6.

Despite these studies, the alkaline-earth analogs Sr_2TiSiO_6 and Ba_2TiSiO_6 remain largely unexplored, both experimentally and theoretically. In this context, the present work provides a systematic first-principles investigation of the structural, mechanical, and optoelectronic properties of silicon-based A_2TiSiO_6 (A = Ca, Sr, Ba) double perovskite oxides. While Ca_2TiSiO_6 has been experimentally realized, the Sr and Ba counterparts are reported

here for the first time as theoretically predicted compounds. This enables a comprehensive analysis of A-site cation substitution (Ca → Sr → Ba), where variations in ionic size and polarizability influence lattice structure, Ti–O–Si hybridization, and electronic interactions, resulting in tunable bandgaps and optical responses. By establishing a direct link between A-site substitution, orbital interactions, and dielectric behavior, this study provides deeper insight beyond conventional trend analysis and supports the rational design of wide-bandgap double perovskites for optoelectronic and renewable energy applications.

2. Results and Discussion

2.1. Structural Properties

The parent compound of the current study, the quaternary silicon-based ordered double perovskite oxide Ca_2TiSiO_6, was first experimentally described by Kurt Leinenweber and John Parise in 1997 [42]. Their experiment proved that Ca_2TiSiO_6 forms with a cubic structure with a space group $Fm\bar{3}m$ (No. 225) and an experimental lattice constant of a_0 = 7.4105 Å. The (1/4, 1/4, 1/4) Wyckoff position is occupied by Ca atoms, Ti atoms occupy the (1/2, 1/2, 1/2) position, Si atoms occupy the (0, 0, 0) and O atoms occupy the (0.2372, 0, 0) position.

Motivated by the experimentally confirmed structural stability and successful synthesis of this parent compound, the present study extends the investigation to the isostructural series A_2TiSiO_6 (A = Ca, Sr, Ba), in which the A-site Ca cation is systematically substituted by Sr and Ba. This substitution strategy enables a direct assessment of how A-site cation size and chemistry influence the structural characteristics of the silicon-based ordered double perovskite framework.

Figure 1 illustrates the cubic unit cell of the silicon-based double perovskite structure using Ca_2TiSiO_6 as the representative model, visualized through a ball-and-stick representation.

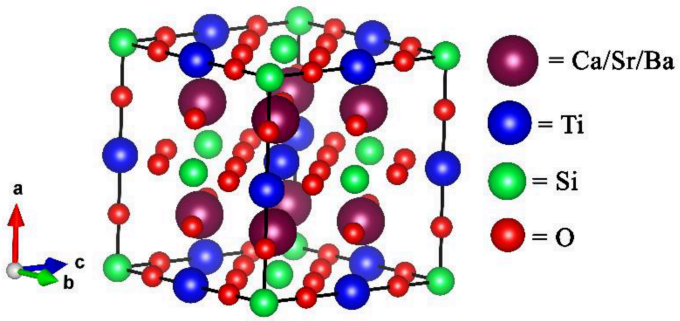


Figure 1. Unit cell of A_2TiSiO_6 (A = Ca, Sr, Ba) compounds.

In the case of the first-principles computations, the crystallographic parameters were used as the starting input structure that were experimentally reported. Complete structural optimization was then done in the context of density functional theory (DFT) with the generalized gradient approximation (GGA) of the exchange correlation functional. During the optimization process, both lattice parameters and internal atomic coordinates were allowed to relax freely until the total energy reached its minimum, yielding the structural ground state of each compound. From the optimized configurations, the equilibrium structural parameters, including the optimized lattice constant (a_0) and the optimized unit cell volume (V) were obtained for all investigated materials.

To determine the thermodynamic stability of the A_2TiSiO_6 (A = Ca, Sr, Ba) compounds, the formation energy (E_f) was determined. Formation energy is also one of the indicators of energetic favorability and it gives an idea whether experimental synthesis could be

feasible. The energy per atom of the formation was calculated by use of the following expression [44]:

$$E_f = \frac{E_{A_2TiSi_6} - n_A \times E_A - n_{Ti} \times E_{Ti} - n_{Si} \times E_{Si} - n_O \times E_O}{N} \quad (1)$$

where $E_{A_2TiSiO_6}$ is the overall energy of the optimum unit cell of the double perovskite oxide, E_A, E_{Ti}, E_{Si}, and E_O is the total energy of the elemental species (A = Ca, Sr, Ba) in their respective reference states. The N_A, N_{Ti}, N_{Si}, and N_0 represent the number of atoms in the formula unit corresponding to the atoms, and N represents the number of atoms in the formula unit, which is 10 in A_2TiSiO_6.

The calculated formation energies of all investigated compounds are negative, as summarized in Table 1, confirming their thermodynamic stability. These negative values indicate that the formation of A_2TiSiO_6 compounds from their constituent elements is energetically favorable, implying that the materials are intrinsically stable and, in principle, experimentally synthesizable.

Table 1. The lattice constant a_0 (Å), the unit cell volume (V), and formation energy (E_f) (eV/atom) for double perovskite of A_2TiSiO_6 (A = Ca, Sr, Ba) compounds.

Compounds	*a* (Å)	*V* (Å^3)	E_f	Ref
Ca_2TiSiO_6	7.4951	421.04	−3.149	This study
	7.4100	406.86		[42]
Sr_2TiSiO_6	7.6292	444.06	−2.824	This study
Ba_2TiSiO_6	7.8372	481.38	−2.324	This study

2.2. Dynamical Stability

Ab initio molecular dynamics (AIMD) simulations were performed at room temperature (300 K) to examine the thermal stability of Ca_2TiSiO_6, Sr_2TiSiO_6, and Ba_2TiSiO_6 through the evolution of their total energies with time (Figure 2). For all three compounds, the total energy fluctuations remain small and well confined within narrow ranges throughout the 10 ps simulation window, indicating stable dynamical behavior under ambient thermal conditions.

Ca_2TiSiO_6 exhibits slightly larger energy fluctuations (~0.0030%) compared to Sr_2TiSiO_6 (~0.0010%) and Ba_2TiSiO_6 (~0.0011%), suggesting relatively higher lattice flexibility or vibrational activity in the Ca-based compound. In contrast, the Sr- and Ba-based systems show more tightly bounded energy variations, reflecting enhanced thermal robustness and stronger lattice stability. The rapid stabilization of the energy profiles after the initial transient region further confirms that all systems quickly reach thermal equilibrium.

The small differences between the maximum, minimum, and mean energies indicate the absence of structural instabilities, bond breaking, or phase transitions over the simulation time scale. These results confirm the dynamical stability of all three compounds at room temperature, validating their structural robustness under realistic thermal conditions. Furthermore, the comparatively lower energy fluctuations observed in Sr_2TiSiO_6 and Ba_2TiSiO_6 suggest that heavier alkaline-earth cations contribute to enhanced lattice stabilization, supporting their suitability for applications where thermal stability is critical. It is also important to note that, in the present work, structural stability has been primarily evaluated using formation energy calculations together with AIMD simulations at 300 K. These approaches provide strong evidence for both thermodynamic and finite-temperature dynamical stability. While additional analyses such as phonon dispersion and Goldschmidt tolerance factor calculations could further complement the stability assessment, they are beyond the current scope of this study and will be addressed in future

work for a more detailed vibrational and structural investigation. Moreover, a comprehensive competing-phase stability analysis has not been performed in the present study; however, it is acknowledged as an important aspect for fully establishing phase stability and experimental feasibility, and will be considered in future work.

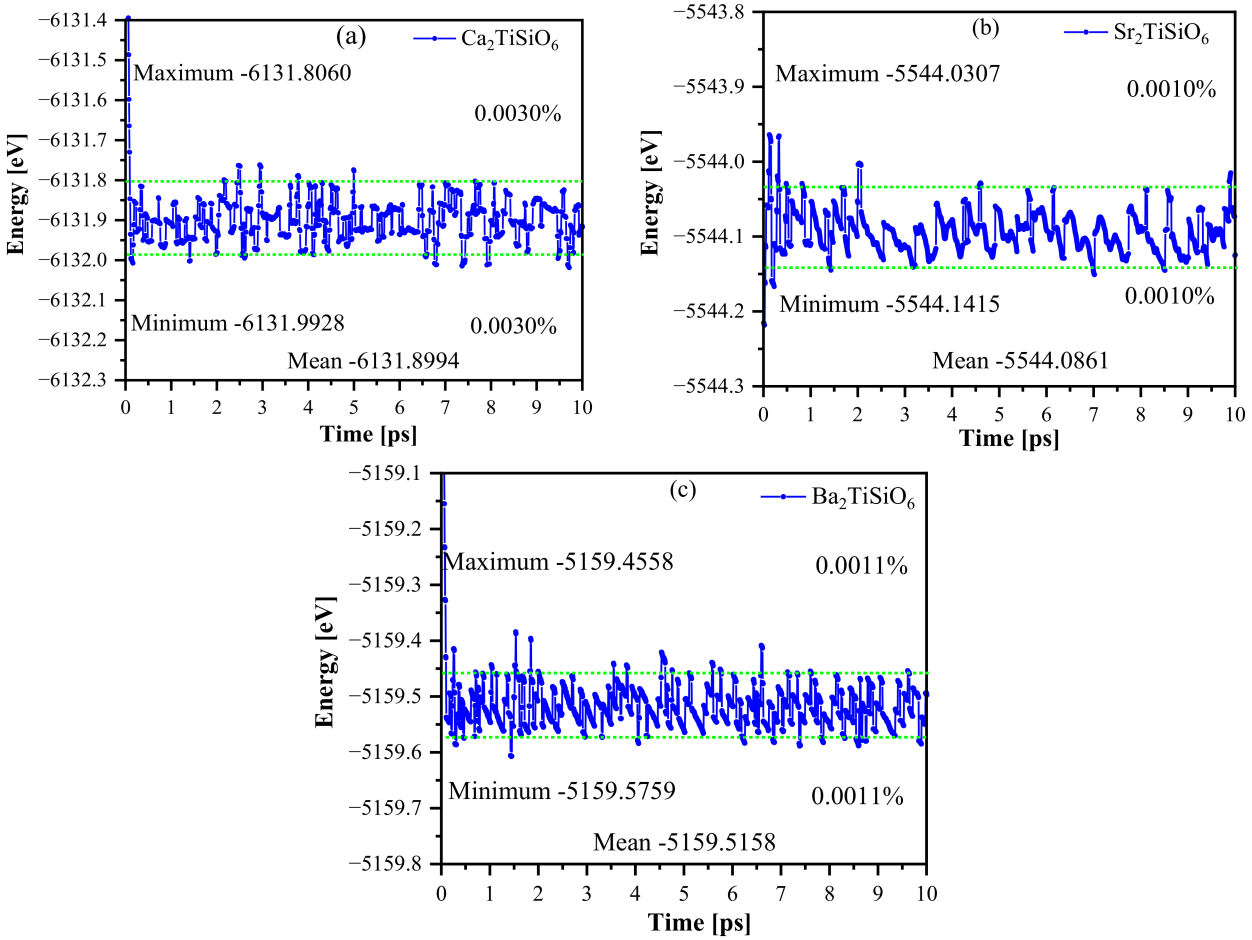


Figure 2. Ab Initio Molecular Dynamics (AIMD) simulations at room temperature (300 K) for total energy fluctuations with time for (**a**) Ca_2TiSiO_6, (**b**) Sr_2TiSiO_6, and (**c**) Ba_2TiSiO_6 compounds.

2.3. Mechanical Properties

The mechanical properties of materials are essential for evaluating their structural stability, reliability, and functional performance during fabrication and practical application. Throughout processing and device integration, materials are frequently exposed to external stresses, making it necessary to understand their elastic behavior and interatomic force interactions at the atomic scale prior to utilization [45]. C_{ij} are the elastic stiffness constants which are the fundamental parameters that directly describe mechanical strength and stability of crystalline solids. Mechanical stability of cubic X_2TiSiO_6 (X = Ca, Sr, Ba) compounds were studied based on the theory of elastic stability of Born–Huang. In the case of a cubic crystal structure, the criteria of mechanical stability are [46]:

$$C_{11} - C_{12} > 0 \quad (2)$$

$$C_{11} + 2C_{12} > 0 \quad (3)$$

$$C_{44} > 0 \quad (4)$$

The conditions provide stability to tetragonal shear deformation, volume compression resistance and stability to shear strain, respectively. A comparatively low C_{12} shows that it is more compressible along the respective crystallographic direction [47].

Table 2 presents the calculated elastic coefficients C_{11}, C_{12}, and C_{44} of A_2TiSiO_6 (A = Ca, Sr, Ba). The compounds all meet the mechanical stability requirements in terms of the equations and attests to their mechanical stability in the cubic form [46]. C_{11} is relatively large, which means that the material is highly resistant to uniaxial deformation, and Ca_2TiSiO_6 has the highest stiffness of the examined materials. The good shear deformation resistance is indicated by the appreciable C_{44} values.

Table 2. Calculated elastic constants (all in GPa) of A_2TiSiO_6 (A = Ca, Sr, Ba) compounds.

Compounds	C_{11}	C_{12}	C_{44}	$C_{11} - C_{12}$	$C_{11} + 2C_{12}$
Ca_2TiSiO_6	341.66	98.33	134.05	243.33	538.32
Sr_2TiSiO_6	302.34	88.39	156.19	391.33	479.72
Ba_2TiSiO_6	275.20	123.52	151.41	398.72	522.24

Moreover, the positive values of $C_{11} - C_{12}$ are indicative that the cubic form is resistant to tetragonal shear deformation, whereas the positive values of $C_{11} + 2C_{12}$ are indicative of a high degree of resistance to uniform compression. Such characteristics indicate high interatomic bonding and mechanically stable cubic phases. The macroscopic elastic parameters were obtained in the form of the Voigt–Reuss–Hill averaging scheme, which is a good compromise between the Voigt and Reuss approximations to determine isotropic mechanical properties [48–50]. The main mechanical descriptors are calculated by the following way:

$$B = \frac{C_{11} + 2C_{12}}{3} \quad (5)$$

$$A = \frac{2C_{44}}{C_{11} - C_{12}} \quad (6)$$

$$\xi = \frac{(C_{11} + 8C_{12})}{7(C_{11} + 2C_{12})} \quad (7)$$

$$Y = \frac{9BG}{3B + G} \quad (8)$$

$$\nu = \frac{3B - 2G}{6B + 2G} \quad (9)$$

$$R_P = \frac{B}{G} \quad (10)$$

$$R_f = \frac{G}{B} \quad (11)$$

$$CP = C_{12} - C_{44} \quad (12)$$

Table 3 shows the calculated values of the bulk modulus (B), shear modulus (G), Young modulus (Y), Poisson ratio (ν), Pugh's ratio (R_P), Frantsevich's ratio (R_f), internal strain factor (ξ), Cauchy pressure (CP), and Zener anisotropy factor (A) of A_2TiSiO_6 (A = Ca, Sr, Ba). The values of the Young's modulus of all compounds are stiffer than the values of the bulk modulus which denote that the compounds will not undergo elastic deformation easily and the compounds are very rigid in their mechanical properties [51].

The increased values of bulk modulus indicate excellent crystal formation and low compressibility. Poisson ratios claim that brittle and ductile materials have a ν of less than 0.26 and over 0.26, respectively [52]. All A_2TiSiO_6 compounds have a calculated value of Poisson's ratio that is less than 0.26, which means that they act brittle. Cauchy

pressure is also in favor of this classification. The negative CP values of all the compounds obtained represent directional (covalent) bonding and brittle nature [53]. In the same manner, the Pugh calculated ratios ($R_P < 1.75$) substantiate brittleness, and the ratios values of Frantsevich's ($R_f > 0.571$) support this finding [51,53].

Table 3. Calculated elastic modulus like the bulk modulus (B), the shear modulus (G), Young's modulus (Y), Poisson's ratio (ν), the Pugh's ratio (R_P), Frantsevich's ratio (R_f), internal strain factor (ξ), Cauchy pressure (CP) and the Zener anisotropy factor (A) for A_2TiSiO_6 (A = Ca, Sr, Ba) compounds.

Compounds	B (GPa)	G (GPa)	Y (GPa)	ν	R_P	R_f	ξ	CP (GPa)	A
Ca_2TiSiO_6	179.44	128.95	312.10	0.210	1.391	0.718	0.299	−35.72	1.101
Sr_2TiSiO_6	159.70	134.21	314.52	0.171	1.189	0.840	0.300	−67.8	1.460
Ba_2TiSiO_6	174.08	114.72	282.18	0.229	1.517	0.659	0.345	−27.98	1.996

The internal strain factor (ξ) is a factor of the resistance of the lattice to internal distortions and is a ratio to the distribution of interatomic forces in the crystal [51]. Values nearer to 1 mean that the crystal is strained in a uniform manner due to stress, whereas values below 1 imply that internal deformation is non-uniform and that the forces are not distributed in an anisotropic manner. In the case of A_2TiSiO_6 compounds, the computed ξ values (Table 3) lie between 0.299, 0.300 and 0.345 and this suggests moderate internal anisotropy. This suggests that the cubic lattice is mechanically stable, but the atomic interactions inside the lattice are a little non-uniform, which is complimentary to the observation of the Zener anisotropy factor ($A \neq 1$) and confirms that these compounds are indeed anisotropic in their elastic behavior at the atomic level. Zener anisotropy factor is not equal to unity in all compounds, which means there is some elastic anisotropy.

Table 4 shows the calculated density (ρ), longitudinal (V_l) and transverse (V_t) and average (V_m) sound velocities as well as the Debye temperature (θ_D) of the cubic double perovskite A_2TiSiO_6 (A = Ca, Sr, Ba) compounds. One of the key thermodynamic parameters is the Debye temperature, which can be used to describe lattice vibrations and is directly connected to such elementary characteristics as the heat capacity, entropy, thermal expansion and thermal conductivity of solids [54]. It also gives an understanding of the interatomic bonding strength and the stiffness of the lattice. The average sound velocity was used to determine the Debye temperature as follows [55]:

$$\theta_D = \frac{h}{k_B}\left[\frac{\left(\frac{3n}{4\pi}\right)N_A\rho}{M}\right]V_m \tag{13}$$

where h is the Planck constant, k_B is the Boltzmann constant, n is the number of atoms in one formula unit, N_A is Avogadro's number, M is the molecular weight, and V_m is the average sound velocity. The longitudinal and transverse sound velocities gave the average sound velocity by:

$$V_m = \left[\frac{1}{3}\left(\frac{1}{v_l^3} + \frac{2}{v_t^3}\right)\right]^{\frac{-1}{3}} \tag{14}$$

Table 4. Calculated density (ρ), transverse, longitudinal, average sound velocity (v_t, v_m, v_l), Debye temperatures (θ_D) and melting temperature (T_m) of Double Perovskite Compounds A_2TiSiO_6 (A = Ca, Sr, Ba) compounds.

Compounds	ρ (kg/m^3)	V_l (m/s)	V_t (m/s)	V_m (m/s)	θ_D (K)	T_m
Ca_2TiSiO_6	6800.96	6230.01	3554.77	3950.49	491.29	2572.25
Sr_2TiSiO_6	3976.49	9400.14	5694.56	6293.59	855.88	2339.84
Ba_2TiSiO_6	5192.39	8075.87	5084.03	5596.12	747.64	2179.46

The transverse and longitudinal sound velocities were calculated from the elastic moduli and density as:

$$V_t = [G/\rho]^{\frac{1}{2}} \text{ and } V_l = [(3B + 4G)/3\rho]^{\frac{1}{2}} \quad (15)$$

As Table 4 demonstrates, Sr_2TiSiO_6 has the greatest longitudinal, transverse and average sound velocities and as expected this compound has the highest Debye temperature of the compounds being studied. Conversely, Ca_2TiSiO_6 exhibits lower sound velocities and lower Debye temperature, which implies a weaker lattice stiffness. Ba_2TiSiO_6 exhibits an intermediate behavior to the compounds of Ca and Sr. Debye temperature contrast is very much related to the sound velocities and the elastic moduli, which prove that lattice dynamics and mechanical rigidity have a strong dependence.

The values of higher Debye temperatures are usually associated with a stronger interatomic bond, phonon frequencies, and thermal conductivity [56,57]. Thus, the Debye temperature of Sr_2TiSiO_6 is relatively high implying higher thermal stability and resistance against lattice vibrations, so it can be used in applications that are characterized by high thermal stability. In general, the analysis of the Debye temperature proves the high mechanical strength and good thermodynamic properties of the cubic A_2TiSiO_6 double perovskites compounds.

Table 4 also indicates the melting temperatures that represent the elastic properties of the materials. Generally, materials that are more elastic rigid have a greater bond among atoms and, therefore, greater thermal resistance. In the case of cubic crystals, we can estimate the melting temperature by the empirical relation [47]

$$T_m = (553 + 5.91C_{11})K \quad (16)$$

which shows that a rise in the elastic constant C_{11} is directly proportional to an increase in the melting temperature. Table 4 illustrates a decreasing trend in the melting temperature (T_m) as the compounds were studied. This practice is explained by differences in elastic stiffness and bonding strength, in which the compounds that have high elastic moduli show better thermal stability.

2.4. Electronic Properties

2.4.1. Band Structure

The electronic band structure of a substance gives a basic understanding of its conductivity and forms a direct correlation between the optical and electronic properties of the material and the crystal structure [58]. The band structure, density of states (DOS) and the density of charge are important parameters used to determine the appropriateness of materials to be used in optoelectronic devices. This section will present and analyze in details the calculated band structure, density of states and charge density distribution of the double perovskite A_2TiSiO_6 (A = Ca, Sr, Ba) compounds by Density Functional Theory (DFT) (Table 5).

Table 5. Calculated bandgap values in (eV) of A_2TiSiO_6 (A = Ca, Sr, Ba) compounds.

Compounds	Ca_2TiSiO_6	Sr_2TiSiO_6	Ba_2TiSiO_6
GGA PBE	2.409	2.309	2.212
HSE06	2.610	2.501	2.372
Nature	Direct	Direct	Direct

Both the GGA–PBE and HSE06 exchange correlation functional were used to compute the electronic bandgaps of A_2TiSiO_6 (A = Ca, Sr, Ba), and the results were summarized

in Table 2. The dispersion of the conduction and valence bands, especially around the high-symmetry points of the first Brillouin zone, is highly desired to determine the nature of the bandgap and the electronic transitions possible. According to Figure 3, the three A_2TiSiO_6 compounds all have a direct bandgap, and both the valence band maximum (VBM) and conduction band minimum (CBM) are at the Γ-point. This direct bandgap property gives it an advantage in obtaining an efficient optical absorption and electron to hole pair generation, which can be used in optoelectronic and photovoltaic devices. Moreover, the bandgaps calculated with the HSE06 put these materials in the wide-bandgap semiconductor regime, and this aspect suggests their applications in the stable optoelectronic devices of ultraviolet and visible light.

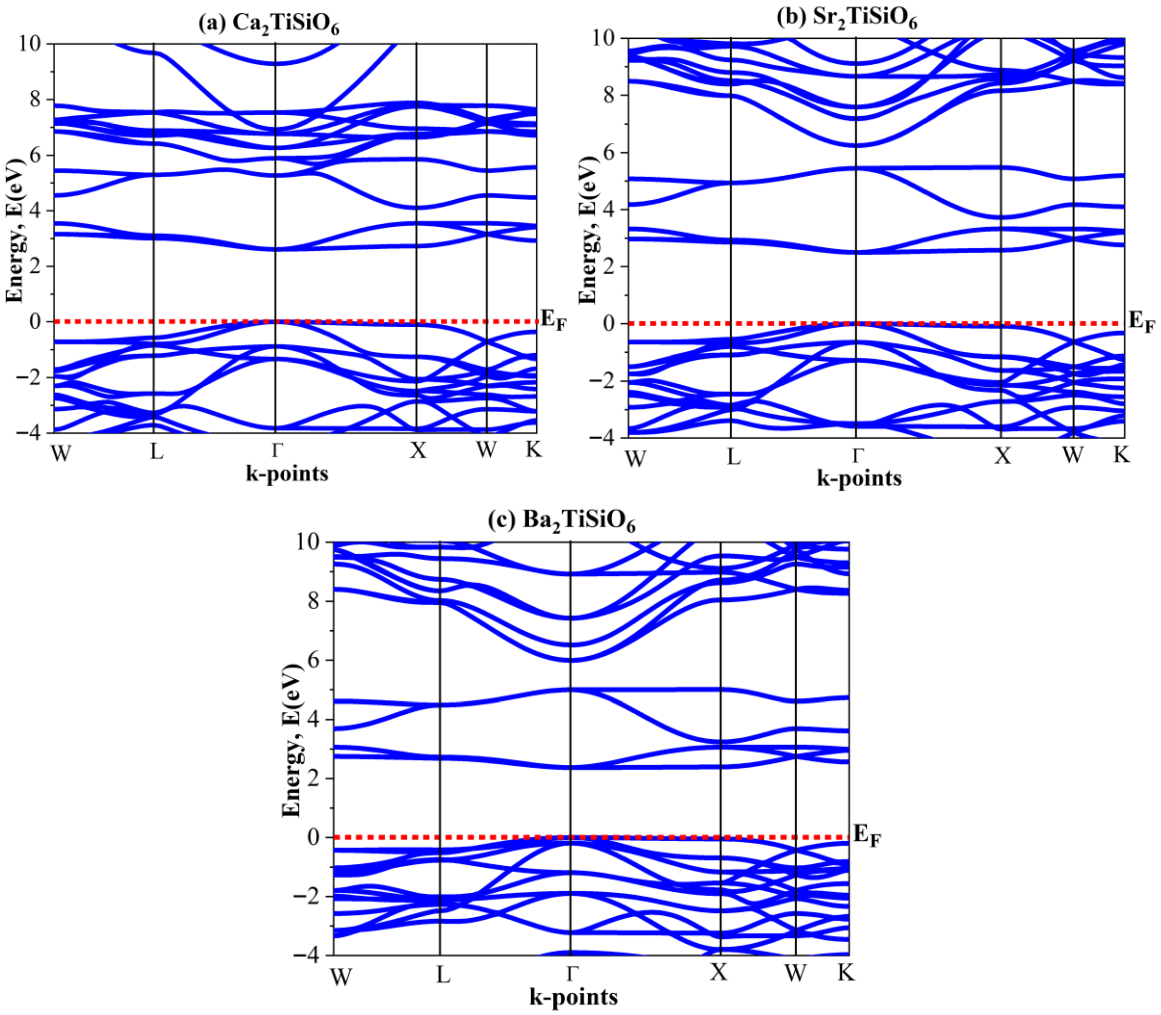


Figure 3. Computed electronic band structures of (**a**) Ca_2TiSiO_6, (**b**) Sr_2TiSiO_6, and (**c**) Ba_2TiSiO_6 compounds.

2.4.2. Density of State (DOS)

Figure 4a–c shows the total and partial density of states (TDOS and PDOS) of A_2TiSiO_6 (A = Ca, Sr, and Ba) calculated with HSE06 hybrid. All those figures indicate clearly that the valence and conduction bands do not intersect the Fermi energy level at all, which proves that all three compounds of the double perovskite are semiconducting.

The total and partial density of state (DOS) shows that there are common electronic characteristics within the series. The O-2*p* states, which are mainly O-2*p* states with some hybridization of Ti-3*d* orbitals are the dominant structure in the region of 0–6 eV, which means that the bond between Ti and O is strong. The alkaline-earth metal atoms (Ca, Sr, and

Ba) play an insignificant role at the Fermi level, which implies that they play an insignificant role in charge transport. Conduction band is above Fermi level, and it is dominated by Ti-3*d* orbital, with minor contributions of Si-*p* and O-*p* orbital. The DOS intensity, especially in the conduction band, shows a gradual increase between Ca_2TiSiO_6 and Ba_2TiSiO_6 that could be explained by increased orbital contributions of the heavier A-site cation. The zero-point energy of the DOS at the Fermi level also proves the semiconducting nature of the systems studied.

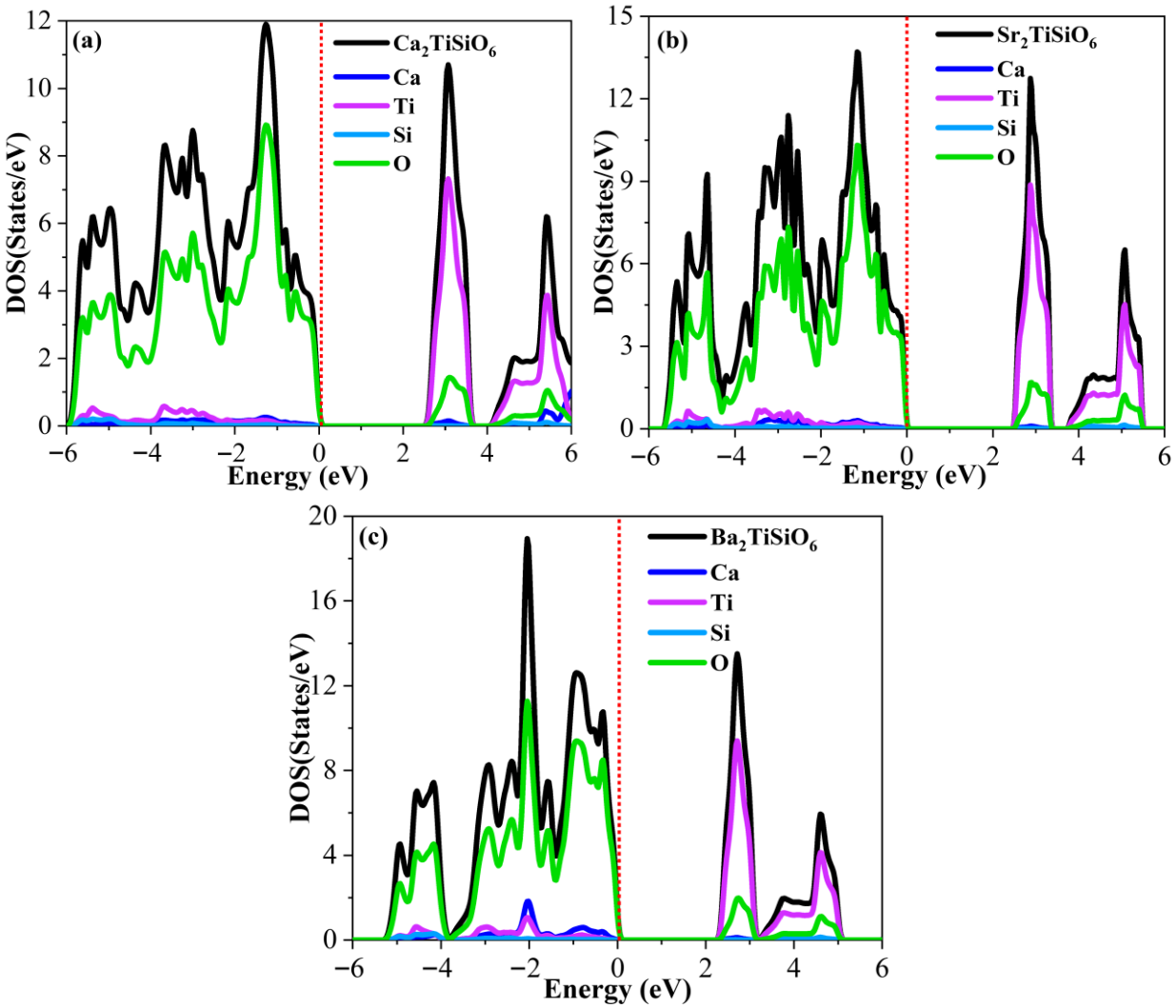


Figure 4. The total and partial density of states of (**a**) Ca_2TiSiO_6, (**b**) Sr_2TiSiO_6, and (**c**) Ba_2TiSiO_6 compounds.

2.4.3. Charge Density

The analysis of charge density is important in the study of the nature of chemical bonding and the mechanism of charge transfer in crystalline materials. Figure 5a–c shows maps of charge density difference $\Delta n\ (r)$ of A_2TiSiO_6 (A = Ca, Sr, Ba), which are a direct measure of the way electronic charge has been redistributed during the formation of the bonds. A large amount of charge accumulation has been observed around the O atoms in all three compounds and the equivalent amount of charge depletion around the A-site cations (Ca/Sr/Ba) and in part around Ti atoms. This indicates that the electron is being transferred off the electropositive atoms in the A-site, along with the Ti atoms to the less electronegative oxygen atoms, which points to the fact that the A–O bonds are predominantly ionic. In the meantime, the accumulated charge along the Ti-O bonds is observable indicating a high

degree of orbital hybridization, indicating the presence of mixed ionic-covalent character of bonds. Gradual charge transfer occurs between Ca_2TiSiO_6 and Ba_2TiSiO_6 which may be explained by the growing ionic radius and electro positivity of the A-site cation.

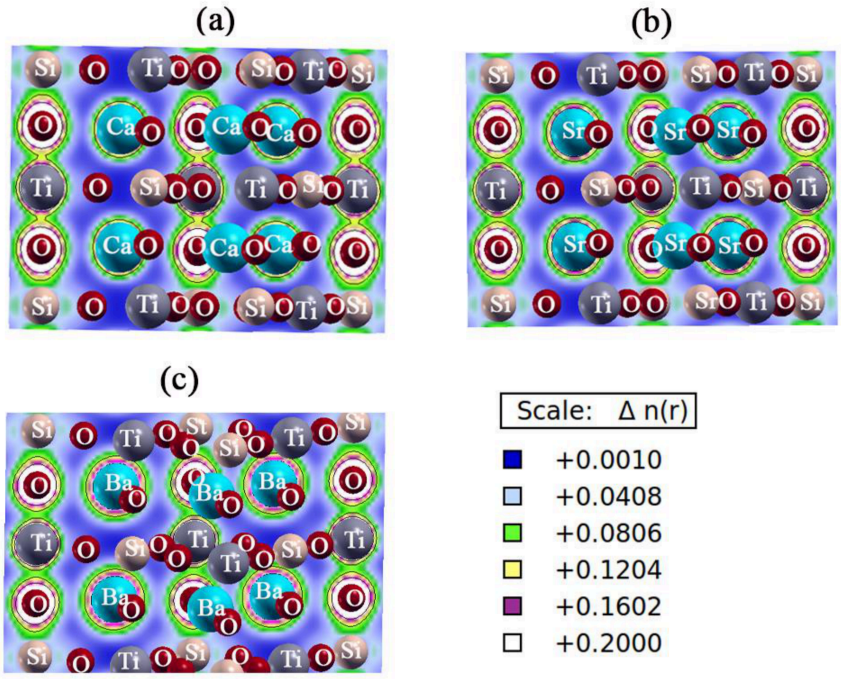


Figure 5. Change density of (**a**) Ca_2TiSiO_6, (**b**) Sr_2TiSiO_6, and (**c**) Ba_2TiSiO_6 compounds.

2.5. Optical Properties

The photovoltaic performance of solar cell devices is strongly governed by the optical properties of the constituent materials, which play a decisive role in the selection of high-efficiency photovoltaic absorbers and are intrinsically linked to their electronic structures [59]. When incident electromagnetic radiations interact with a material, they cause optical responses that determine the efficiency of photon absorption and energy conversion [60,61]. Here, a high optical absorption and a high dielectric constant is very desirable. In this work, all optical properties have been calculated using the HSE06 hybrid functional to ensure improved accuracy in describing the electronic structure and related optical response. In the linear response theory, optical properties of a material are characterized by the complex, frequency dependent dielectric function $\varepsilon(\omega)$, which is given by [61,62]:

$$\varepsilon(\omega) = \varepsilon_1(\omega) + i\varepsilon_2(\omega) \tag{17}$$

where $\varepsilon_1(\omega)$ and $\varepsilon_2(\omega)$ are the real and imaginary components of the dielectric tensor, respectively. The real component $\varepsilon_1(\omega)$ represents the polarization response of the material to the incident electromagnetic field, and the imaginary component $\varepsilon_2(\omega)$ is the absorption of electromagnetic radiation [63,64]. Fundamental material properties such as electronic band structure, lattice vibrations, impurity states and excitonic effects can also be determined through optical properties [60,61]. The Kramers–Kronig relations relate the real and imaginary part of the dielectric function [65]:

$$\varepsilon_1(\omega) = \frac{2}{\pi}\rho\int_0^\infty \frac{\omega'^2\varepsilon_2\omega}{\omega'^2 - \omega^2} \tag{18}$$

$$\varepsilon_2(\omega) = \frac{-2}{\pi}\rho\int_0^\infty \frac{\omega'^2\varepsilon_2\omega}{\omega'^2 - \omega^2} \tag{19}$$

where ρ represents the principal of the integral.

Based on the dielectric function calculated, a number of optical parameters were obtained of A_2TiSiO_6 (A = Ca, Sr, Ba) such as reflectivity $R(\omega)$, the refractive index $n(\omega)$, the extinction coefficient $k(\omega)$, the optical conductivity $\sigma(\omega)$, the electron energy loss function $L(\omega)$, and absorption coefficient $\alpha(\omega)$ over the photon energy range 0–25 eV. The HSE06 hybrid functional was used to calculate all the results. The dielectric function is connected with the optical constants in the following way:

$$\sigma(\omega) = \frac{\omega}{4\pi}\varepsilon_2(\omega) \tag{20}$$

$$n(\omega) = \sqrt{\frac{|\varepsilon(\omega)| + \varepsilon_1(\omega)}{2}} \tag{21}$$

$$K(\omega) = \sqrt{\frac{|\varepsilon(\omega)| - \varepsilon_1(\omega)}{2}} \tag{22}$$

$$L(\omega) = \frac{\varepsilon_2}{\varepsilon_1^2 + \varepsilon_2^2} \tag{23}$$

$$R(\omega) = \frac{(n-1)^2 + k^2}{(n+1)^2 + k^2} \tag{24}$$

$$\alpha(\omega) = \sqrt{2}\omega\left(\frac{\varepsilon_1(\omega)^2 + \varepsilon_2(\omega)^2 - \varepsilon_1(\omega)}{2}\right)^{\frac{1}{2}} \tag{25}$$

Importantly, the spectral features of $\varepsilon_2(\omega)$ are directly associated with interband transitions between O-2p dominated valence band states and Ti-3*d* dominated conduction band states, as confirmed from the electronic density of states analysis. Thus, the major peaks in the dielectric spectra can be explicitly correlated with these orbital-resolved transitions.

The interband electronic transitions in the investigated alkaline-earth titanate silicates A_2TiSiO_6 (A = Ca, Sr, Ba) contribute directly to their calculated dielectric functions and are intrinsically linked to their electronic band structures. Figure 6a presents the real part of the dielectric function, $\varepsilon_1(\omega)$, as a function of photon energy. The low-energy (static) limit of this function yields the static dielectric constant, $\varepsilon_1(0)$, which is directly proportional to the electronic polarizability of the materials. The $\varepsilon_1(0)$ values at rest are 4.68, 4.89, and 5.47 of $Ca_2Ti\ SiO_6$, Sr_2TiSiO_6, and $Ba_2Ti\ SiO_6$ respectively. The growing trend shows that the polarizability improves as the ionic radius of the alkaline-earth metal increases. The gradual increase in $\varepsilon_1(0)$ from Ca to Ba reflects enhanced electronic polarizability due to the larger ionic radius and more delocalized electronic cloud, which is beneficial for dielectric and optoelectronic device applications. This large dispersion at low photon energies can be primarily connected with the transitions which depend on the bandgap and the appearance of negative $\varepsilon_1(\omega)$ at higher energies indicates plasma-like behavior and high reflectivity. The energy range where $\varepsilon_1(\omega)$ becomes negative corresponds to the screened plasma frequency, indicating strong collective oscillations of conduction electrons and marking the transition from dielectric to metallic-like optical response.

The imaginary component of the dielectric function describes the behavior of a substance to incident electromagnetic radiation and is directly related to interband electronic transfers between occupied states of the valence band and unoccupied states of the conduction band [66]. More specifically, the first onset of $\varepsilon_2(\omega)$ corresponds to the fundamental direct bandgap transition (VBM → CBM), while the higher-energy peaks originate from deeper O-2p states to higher Ti-3d/Si-p conduction bands. This element is commonly employed to determine the optical gap because optical gap is equal to onset $\varepsilon_2(\omega)$, which is the minimum photon energy necessary to create an electron–hole pair [67]. All the

excitonic peaks recorded to all the studied compounds are within the bandgap energy region. Whenever the energy range of visible light coincides with the excitonic transition energy, the material will have low reflectivity and high absorption coefficient meaning the material can be useful in optoelectronics application [68]. The imaginary component of the dielectric function, $\varepsilon_2(\omega)$ of A_2TiSiO_6 is shown in Figure 6b. Ca_2TiSiO_6 exhibits the highest absorption peak with a value of 7.29 at 4.09 eV, while Sr_2TiSiO_6 shows a maximum peak of 6.44 at 3.91 eV, and Ba_2TiSiO_6 displays a peak value of 6.56 at 3.64 eV. These peak positions fall within the near-UV region and correspond to strong O-2p $\rightarrow$ Ti-3d charge transfer transitions, which dominate the optical response in oxide perovskites. The red-shift of peak positions from Ca to Ba indicates bandgap narrowing and enhanced optical activity in the visible–UV boundary region. The gradual loss of the peak positions of Ca_2TiSiO_6 to Ba_2TiSiO_6 is evidence of the alkaline-earth cation changing the electronic structure.

The refractive index of the material at zero photon energy is equal to the static refractive index [69]. Figure 6c indicates that the calculated static refractive indices are 2.17 of Ca_2TiSiO_6, 2.20 of Sr_2TiSiO_6 and 2.34 of Ba_2TiSiO_6. The three compounds have a sharp peak in the index of refraction at 3–3.1 eV, rising to a value of about 2.9–3.0, in the visible–near-ultraviolet part of the spectrum. This aspect means that they could be applicable in solar cells and optoelectronics. Beyond this range, the refractive index gradually decreases with increasing photon energy, reaching a minimum of 0.5–0.8 near 22–25 eV, suggesting that these materials become increasingly transparent in the extreme ultraviolet region.

Optical conductivity $\sigma(\omega)$ captures formation of the free charge carriers through absorption of incident photons [70,71] and directly proportional to the imaginary part of the dielectric function [69]. As it can be seen in Figure 6d, the three perovskites all have a zero optical conductivity at low photon energies. As the energy increases, σ increases and possesses clear peaks that are related to solid electronic transitions. Particularly, Ca_2TiSiO_6 has a maximum of 7.04 at 17.59 eV, Sr_2TiSiO_6 peaks at 11.42 at 23.14 eV and Ba_2TiSiO_6 peaks at 9.38 at 18.54 eV. These peaks represent the presence of high levels of photon absorption and imply the possible optoelectronic behavior in the ultraviolet energy spectrum.

Figure 6e shows the optical absorption coefficient, $\alpha(\omega)$, versus the photon energy of A_2TiSiO_6. In the low-energy region, all three compounds exhibit nearly zero absorption, indicating optical transparency at low photon energies. The absorption coefficient grows exponentially with the photon energy, and this is indicative of the interband electronic transitions. Ca_2TiSiO_6, Sr_2TiSiO_6, and Ba_2TiSiO_6 show the first prominent absorption peaks at 4.26 eV (0.66×10^6 cm^{-1}), 3.99 eV (0.58×10^6 cm^{-1}), and 3.76 eV (0.54×10^6 cm^{-1}), respectively. The average maximum absorption coefficients are 2.2×10^6 cm^{-1} at 17.76 eV with Ca_2TiSiO_6, 4.1×10^6 cm^{-1} at 24.37 eV with Sr_2TiSiO_6, and 3.1×10^6 cm^{-1} at 19.56 eV with Ba_2TiSiO_6. The weakest absorption intensity is observed in Ca_2TiSiO_6 and the strongest absorption is observed in Sr_2TiSiO_6 and Ba_2TiSiO_6 with coefficients of the order of 10^6 cm^{-1}. At increased photon energies, $\alpha(\omega)$ exhibits strong oscillatory character and this character is because of complicated high-energy electronic transitions in the conduction bands.

Figure 6f depicts the energy loss function $L(\omega)$. At low energy, the loss of all compounds is negligible, which means that there is a weak loss of energy. Ca_2TiSiO_6, Sr_2TiSiO_6 and Ba_2TiSiO_6 have the values of the static energy losses as 2.56 eV, 2.59 eV and 2.24 eV, respectively. In the intermediate energy range, several loss peaks appear due to interband transitions and plasmon excitations. At higher energies, pronounced loss maxima are observed, with Ca_2TiSiO_6 exhibiting the highest loss intensity of about 1.20 at 22.29 eV, followed by Ba_2TiSiO_6 with a peak of 0.85 at 23.98 eV, and Sr_2TiSiO_6 showing a lower maximum of 0.75 at 18.59 eV. These differences show the effect of the alkaline-earth cations on the plasmonic response of the materials.

The amplitude of incident and reflected electromagnetic waves are used to compute the reflection coefficient $R(\omega)$ [72]. The relatively low reflectivity values (~0.13–0.16 in the visible region) indicate minimal optical losses due to reflection, which is desirable for maximizing absorption in photovoltaic devices [73]. The obtained reflectivity spectra $R(\omega)$ are demonstrated in Figure 6g. The static reflectivity values are approximately 0.13 for Ca_2TiSiO_6, 0.14 for Sr_2TiSiO_6, and 0.16 for Ba_2TiSiO_6. All three compounds in the low-energy region (below about 5 eV) show a slow rise in reflectivity, which is then followed by a sharp rise at about 3–4 eV, attributed to intense optical transitions at the band edge. The reflectivity oscillates in intermediate energy (5–15 eV) region with many peaks and dales, which is the result of numerous interband transitions. Ba_2TiSiO_6 tells a much-improved reflectivity at higher energies (above ~15 eV) with a pronounced peak at 19–20 eV, but Sr_2TiSiO_6 shows a sharp rise ~22 eV and becomes the highest of the three compounds. On the contrary, Ca_2TiSiO_6 retains relatively low reflectivity in this high energy region.

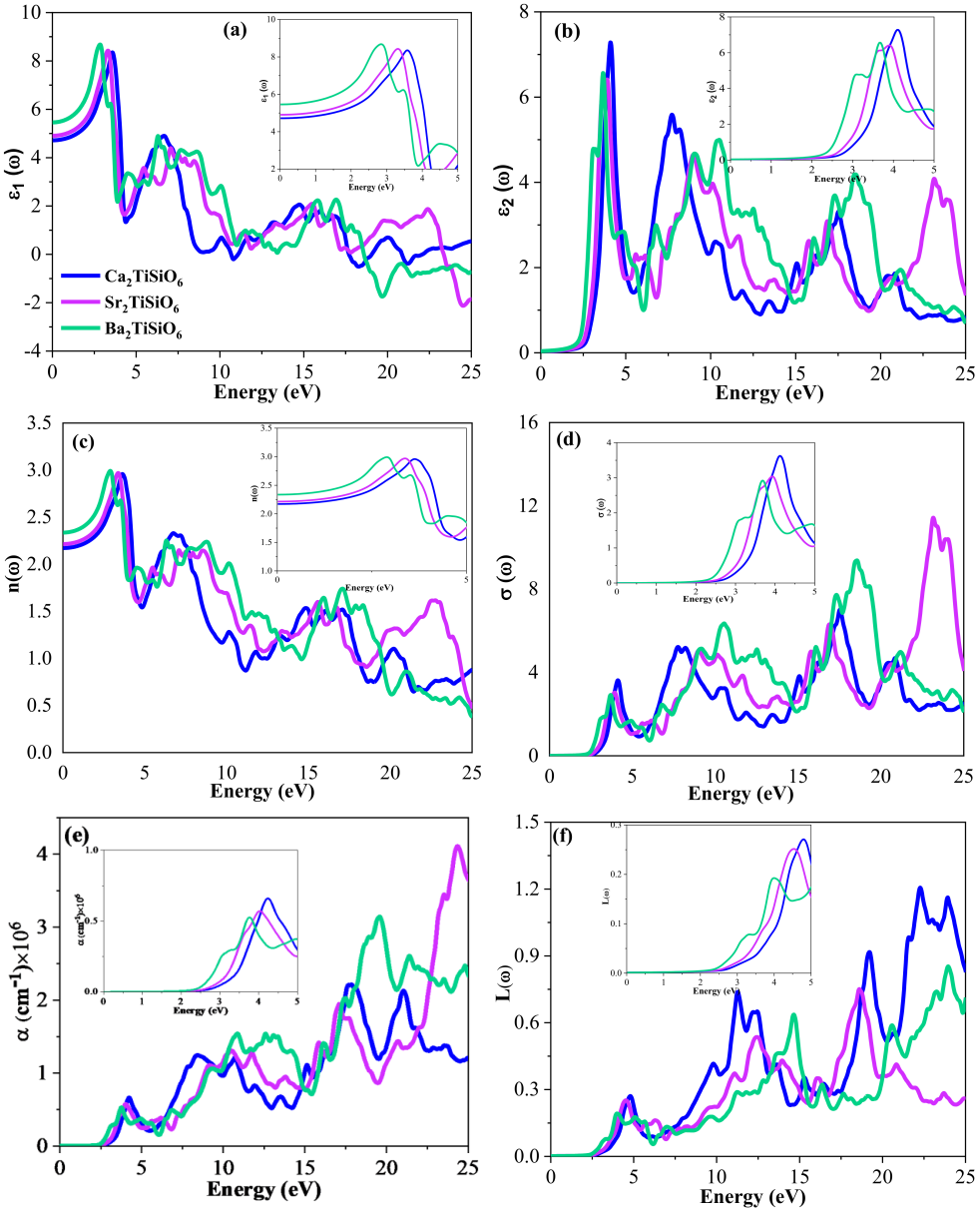


Figure 6. *Cont.*

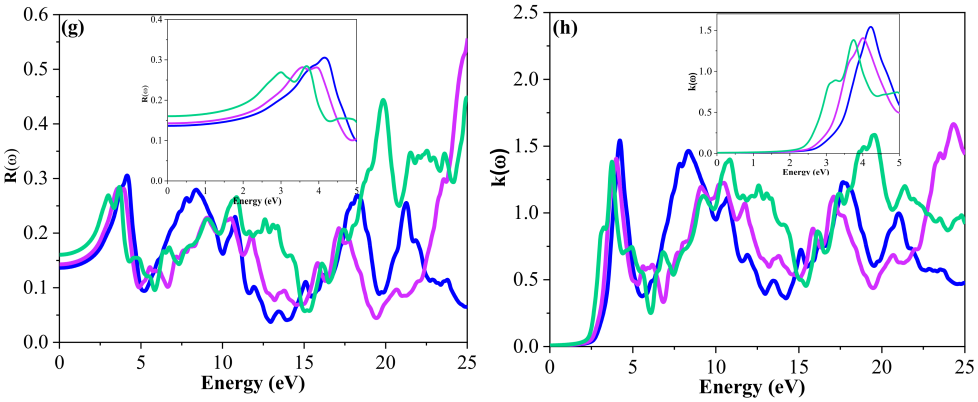


Figure 6. Calculated optical parameters (**a**) Real dielectric part ($\varepsilon_1(\omega)$), (**b**) Imaginary dielectric part ($\varepsilon_2(\omega)$), (**c**) Refractive index ($n(\omega)$), (**d**) Conductivity ($\sigma(\omega)$), (**e**) Absorption coefficient ($\alpha(\omega)$), (**f**) Loss function ($L(\omega)$), (**g**) Reflectivity ($R(\omega)$) and (**h**) Extinction coefficient ($k(\omega)$) of A_2TiSiO_6 (A = Ca, Sr, Ba) compounds.

The extinction coefficient is a property of a material which describes its capability to absorb incident light, a major aspect of optoelectronic materials [62,74]. It also defines how electromagnetic radiations attenuate with the material at a given wavelength [75]. The extinction coefficient $k(\omega)$ of the compounds studied is depicted in Figure 6h. In the low-energy region (below ~3 eV), $k(\omega)$ is nearly zero for all compounds, indicating negligible optical absorption. A steep rise in $k(\omega)$ takes place in the visible to near-UV spectrum, which is associated with the beginning of interband electronic transitions. Ca_2TiSiO_6 absorbs strongly in the long wavelengths with a maximum extinction coefficient of about 1.54 at 4.23 0 eV. At higher energies Sr_2TiSiO_6 has its maximum of about 1.66 at 24.34 eV and the value of Ba_2TiSiO_6 is sharp 1.58 at 19.52 eV. The variation in the positions and strengths of the various compounds at their peaks shows the influence of the alkaline-earth cations on the optical absorption of the compounds.

3. Materials and Methods

The physical properties of the cation-decorated double perovskites A_2TiSiO_6 (A = Ca, Sr, Ba) were studied by the use of first-principles calculations based on the framework of Density Functional Theory (DFT) through the Quantum ESPRESSO version 7.4.1. package [76,77]. Plane-wave pseudo potential method was used and the interaction between the valence electrons and cores of the ion was modeled by the use of ultrasoft pseudopotentials which were chosen to form an optimal balance of efficiency and accuracy in computations. All calculations were performed in a non-spin-polarized framework, and test spin-polarized calculations confirmed a zero net magnetic moment for all compounds, indicating a non-magnetic ground state. The optimization of the structure was carried out by means of the generalized gradient approximation (GGA) in which the Perdew–Burke–Ernzerhof (PBE) exchange correlation functional was used [78]. The lattice parameters and internal atomic coordinates were also completely relaxed until the total energy reached its minimum. The convergence tests were used to select a plane-wave kinetic energy cutoff of 60 Ry and a Monkhorst packing k-point mesh of 10 × 10 × 10, which gave reliable and converged results on all compounds investigated. To achieve more precise electronic band structures and optical properties, the HSE06 hybrid functional [79] was used and the well-known bandgap underestimation of the standard GGA functional sets were overcome. The energy strain method of arriving at elastic constants as in the thermo_pw module [80], allowed the determination of the mechanical stability and elastic behavior. In general, the given multiscale computational methodology offers an in-depth insight into the structural, me-

chanical, electronic, and optical characteristics of A_2TiSiO_6 double perovskites, which may be utilized in optoelectronics.

4. Conclusions

A systematic first-principles investigation of the structural, dynamical, mechanical, electronic, and optical properties of cubic quaternary silicon-based double perovskite oxides A_2TiSiO_6 (A = Ca, Sr, Ba) was performed within density functional theory using the Quantum ESPRESSO package, employing both PBE–GGA and HSE06 exchange correlation functionals. Structural optimization together with ab initio molecular dynamics simulations confirm the structural integrity and dynamical stability of all compounds in the cubic phase.

The calculated elastic constants satisfy the mechanical stability criteria, indicating that A_2TiSiO_6 compounds are mechanically stable, elastically anisotropic, and brittle in nature, with bonding characteristics dominated mainly by covalent interactions. Electronic band structure calculations reveal that all studied materials exhibit direct wide-bandgap semiconducting behavior.

Furthermore, the strong optical absorption in the visible–ultraviolet region, along with positive dielectric constants and appreciable refractive indices, highlights their potential for optoelectronic applications such as ultraviolet photodetectors, light-emitting devices, and photovoltaic absorbers. Overall, the results demonstrate a clear correlation between A-site cation chemistry and the resulting physical properties, suggesting that A_2TiSiO_6 double perovskites are promising candidates for advanced optoelectronic and photovoltaic technologies.

Author Contributions: Conceptualization, Ł.S. and M.G.; methodology, Ł.S. and M.G.; software, Ł.S.; validation, Ł.S. and M.G.; formal analysis, Ł.S. and M.G.; investigation, Ł.S., M.G. and K.M.-G.; resources, Ł.S.; data curation, Ł.S.; writing—original draft preparation, Ł.S. and M.G.; writing—review and editing, Ł.S. and K.M.-G.; visualization, Ł.S.; supervision, Ł.S.; project administration, Ł.S.; funding acquisition, Ł.S. All authors have read and agreed to the published version of the manuscript.

Funding: This research received no external funding.

Institutional Review Board Statement: Not applicable.

Informed Consent Statement: Not applicable.

Data Availability Statement: The original contributions presented in this study are included in the article. Further inquiries can be directed to the corresponding author.

Conflicts of Interest: The authors declare no conflicts of interest.

References

1. Bhattacharjee, S.; Parida, R.K.; Parida, B.N. Investigation of multifunction features of double perovskite oxide A_2FeVO_6 (where A = Ba, Ca). *Phys. B Condens. Matter* **2023**, *659*, 414849. [CrossRef]
2. Dar, S.A.; Murtaza, G.; Zelai, T.; Nazir, G.; Alkhaldi, H.; Albalawi, H.; Kattan, N.A.; Irfan, M.; Mahmood, Q.; Mahmoud, Z. Study of structural, electronic, magnetic, and optical properties of A_2FeMnO_6 (A = Ba, La) double perovskites, experimental and DFT analysis. *Colloids Surf. A Physicochem. Eng. Asp.* **2023**, *664*, 131145. [CrossRef]
3. Huang, Z.; Luo, P.; Jia, S.; Zheng, H.; Lyu, Z. A sulfur-doped carbon-enhanced $Na_3V_2(PO_4)_3$ nanocomposite for sodium-ion storage. *J. Phys. Chem. Solids* **2022**, *167*, 110746. [CrossRef]
4. Yi, K.; Tang, Q.; Wu, Z.; Gu, J.; Zhu, X. Structural, magnetic, and electrical transport properties of half-metallic double perovskite La_2CrNiO_6 oxides. *J. Alloys Compd.* **2023**, *933*, 167742. [CrossRef]
5. Mishra, S.; Choudhary, R.N.P.; Parida, S.K. A multifunctional transition metal based double perovskite $Ba_2(FeW)O_6$: Structural, microstructural, optical, electrical and ferroelectric properties. *Ceram. Int.* **2023**, *49*, 22702–22717. [CrossRef]
6. Katayama, T.; Mo, S.; Chikamatsu, A.; Kurauchi, Y.; Kumigashira, H.; Hasegawa, T. Half-Metallicity and Magnetic Anisotropy in Double-Perovskite $GdBaCo_2O_6$ Films Prepared via Topotactic Oxidation. *Chem. Mater.* **2023**, *35*, 1295–1300. [CrossRef]

7. Huang, Z.; Luo, P.; Wu, Q.; Zheng, H. Constructing one-dimensional mesoporous carbon nanofibers loaded with $NaTi_2(PO_4)_3$ nanodots as novel anodes for sodium energy storage. *J. Phys. Chem. Solids* **2022**, *161*, 110479. [CrossRef]
8. Chen, X.-F. Periodic Density Functional Theory (PDFT) Simulating Crystal Structures with Microporous CHA Framework: An Accuracy and Efficiency Study. *Inorganics* **2023**, *11*, 215. [CrossRef]
9. Zhang, B.; Zhang, S.; Han, H.; Tang, K.; Xia, C. Cobalt-Free Double Perovskite Oxide as a Promising Cathode for Solid Oxide Fuel Cells. *ACS Appl. Mater. Interfaces* **2023**, *15*, 8253–8262. [CrossRef]
10. Singh, P.; Kumar, A. Device engineering of double perovskite based solar cells towards high-performance, eco-friendly solar cells. *Opt. Quantum Electron.* **2023**, *55*, 304. [CrossRef]
11. Hossain, A.; Alharbi, H.F.; Hasan, M.M.; Selvanathan, V.; Islam, M.d.A.; Homyra, S.; Hasan, A.K.M.; Haque, M.; Shahiduzzaman, M.; Uddin, M. First-principles investigation of electronic, optical, and thermal properties of zintl phase MgX_2N_2 (X = Be, Ca, Sr) for optoelectronic applications: A DFT study. *Comput. Condens. Matter* **2025**, *43*, e01042. [CrossRef]
12. Bairwa, J.K.; Rani, M.; Kamlesh, P.K.; Singh, R.; Rani, U.; Al-Qaisi, S.; Kumar, T.; Kumari, S.; Verma, A.S. Modeling and simulation of multifaceted properties of X_2NaIO_6 (X = Ca and Sr) double perovskite oxides for advanced technological applications. *J. Mol. Model.* **2023**, *29*, 379. [CrossRef]
13. Irfan, M.; Murtaza, G.; Muhammad, N.; Tahir, S.; Raza, H.H.; Sabir, B.; Iftikhar, M.; Sharif, S. Experimental and theoretical studies of structural, electronic and magnetic properties of RE_2NiCrO_6 (RE = ce, Pr and Nd) double perovskites. *Phys. E Low-Dimens. Syst. Nanostructures* **2023**, *148*, 115635. [CrossRef]
14. Li, X.; Aftab, S.; Hussain, S.; Kabir, F.; Henaish, A.M.A.; Al-Sehemi, A.G.; Pallavolu, M.R.; Koyyada, G. Dimensional diversity (0D, 1D, 2D, and 3D) in perovskite solar cells: Exploring the potential of mixed-dimensional integrations. *J. Mater. Chem. A* **2024**, *12*, 4421–4440. [CrossRef]
15. Liu, Y.P.; Fuh, H.R.; Wang, Y.K. Study of the half-metallic materials double perovskites Sr_2ZnBO_6 (B = Tc, Re, Ru, Os, Co, Pd, and Au) via first-principle calculations. *J. Magn. Magn. Mater.* **2013**, *341*, 25–29. [CrossRef]
16. Philipp, J.B.; Majewski, P.; Alff, L.; Erb, A.; Gross, R.; Graf, T.; Brandt, M.S.; Simon, J.; Walther, T.; Mader, W.; et al. Structural and doping effects in the half-metallic double perovskite A_2CrWO_6 (A = Sr, Ba, and Ca). *Phys. Rev. B* **2003**, *68*, 144431. [CrossRef]
17. Li, M.; Retuerto, M.; Deng, Z.; Stephens, P.W.; Croft, M.; Huang, Q.; Wu, H.; Deng, X.; Kotliar, G.; Sánchez-Benítez, J.; et al. Giant Magnetoresistance in the Half-Metallic Double-Perovskite Ferrimagnet Mn_2FeReO_6. *Angew. Chem. Int. Ed.* **2015**, *54*, 12069–12073. [CrossRef]
18. Zhang, J.; Ji, W.-J.; Xu, J.; Geng, X.-Y.; Zhou, J.; Gu, Z.-B.; Yao, S.-H.; Zhang, S.-T. Giant positive magnetoresistance in half-metallic double-perovskite Sr_2CrWO_6 thin films. *Sci. Adv.* **2017**, *3*, e1701473. [CrossRef] [PubMed]
19. Liu, R.; Kliem, B.; Titov, V.S.; Chen, J.; Wang, Y.; Wang, H.; Liu, C.; Xu, Y.; Wiegelmann, T. Structure, Stability, and Evolution of Magnetic Flux Ropes from the Perspective of Magnetic Twist. *Astrophys. J.* **2016**, *818*, 148. [CrossRef]
20. Wei, X.-P.; Cao, T.-Y.; Sun, X.-W.; Gao, Q.; Gao, P.; Gao, Z.-L.; Tao, X.-M. Structural, electronic, and magnetic properties of quaternary Heusler CrZrCoZ compounds: A first-principles study. *Chin. Phys. B* **2020**, *29*, 077105. [CrossRef]
21. Teli, N.A.; Mir, S.H.; Sirajuddeen, M.M.S.; Banu, I.S. A computational study of TiHfPtZ (Z = Al, Ga, In) quaternary heusler compounds for spintronics applications. *Phys. Scr.* **2024**, *99*, 025974. [CrossRef]
22. Tang, Q.; Zhu, X. Half-metallic double perovskite oxides: Recent developments and future perspectives. *J. Mater. Chem. C* **2022**, *10*, 15301–15338. [CrossRef]
23. Saha-Dasgupta, T. Double perovskites with 3d and 4d/5d transition metals: Compounds with promises. *Mater. Res. Express* **2020**, *7*, 014003. [CrossRef]
24. Vasala, S.; Karppinen, M. $A_2B'B''O_6$ perovskites: A review. *Prog. Solid State Chem.* **2015**, *43*, 1–36. [CrossRef]
25. Alam, M.; Chatterjee, S. B-site order/disorder in $A_2BB'O_6$ and its correlation with their magnetic property. *J. Phys. Condens. Matter* **2023**, *35*, 223001. [CrossRef]
26. Khandy, S.A.; Gupta, D.C. Study of ferromagnetism, spin-polarization, thermoelectrics and thermodynamics of layered perovskite Ba_2FeMnO_6 under pressure and temperature. *J. Phys. Chem. Solids* **2019**, *135*, 109079. [CrossRef]
27. Ullah, R.; Ali, M.A.; Haq, B.U.; Khan, A.; Mahmood, Q.; Murtaza, G. Exploring electronic, structural, magnetic and thermoelectric properties of novel Ba_2EuMoO_6 double perovskite. *Mater. Sci. Semicond. Process.* **2022**, *137*, 106218. [CrossRef]
28. Haid, S.; Matougui, M.; Benatmane, S.; Bouadjemi, B.; Houari, M.; Zitouni, A.; Lantri, T.; Bentata, S. Predictive Study of the Rare Earth Double Perovskite Oxide Ba_2ErReO_6 and the Influence of the Hubbard Parameter U on its Half-Metallicity. *J. Supercond. Nov. Magn.* **2021**, *34*, 2893–2903. [CrossRef]
29. Mandal, T.K.; Poltavets, V.V.; Croft, M.; Greenblatt, M. Synthesis, structure and magnetic properties of $A_2MnB'O_6$ (A = Ca, Sr; B′ = Sb, Ta) double perovskites. *J. Solid State Chem.* **2008**, *181*, 2325–2331. [CrossRef]
30. Rameshe, B.; Murugan, R.; Palanivel, B. First principle study on electronic structure, structural phase stability, optical and vibrational properties of Ba_2ScMO_6 (M = Nb, Ta). *Int. J. Mod. Phys. B* **2016**, *30*, 1550246. [CrossRef]
31. Cheah, M.C.L.; Kennedy, B.J. Synthesis and structures of chromium double perovskites A_2CrTaO_6 (A = Sr, Ca). *Phys. B Condens. Matter* **2006**, *385–386*, 184–186. [CrossRef]

32. Zhang, S.; Shi, L. Pressure-dependent structural, elastic, electronic and vibrational studies of Ba_2InMO_6 (M = Ta, Nb) from first principles. *Comput. Mater. Sci.* **2018**, *142*, 99–107. [CrossRef]
33. Ghosh, B.; Halder, S.; Shannigrahi, S.; Sinha, T.P. X-ray photoelectron spectroscopic study and electronic structure of double-perovskites A_2SmTaO_6 (A = Ba, Sr, Ca). *Solid State Sci.* **2017**, *67*, 114–118. [CrossRef]
34. Toro, C.E.D.; Rodríguez, M.J.A.; Téllez, D.A.L.; Salazar, N.O.M.; Roa-Rojas, J. First principles study of the structural and electronic properties of double perovskite Ba_2YTaO_6 in cubic and tetragonal phases. *Phys. B Condens. Matter* **2014**, *455*, 18–21. [CrossRef]
35. Saad, H.-E.M.M.; Elhag, A. DFT study on the crystal, electronic and magnetic structures of tantalum based double perovskite oxides Ba_2MTaO_6 (M = Cr, Mn, Fe) via GGA and GGA + U. *Results Phys.* **2018**, *9*, 793–805. [CrossRef]
36. Sheikh, M.S.; Ghosh, D.; Dutta, A.; Bhattacharyya, S.; Sinha, T.P. Lead free double perovskite oxides Ln_2NiMnO_6 (Ln = La, Eu, Dy, Lu), a new promising material for photovoltaic application. *Mater. Sci. Eng. B* **2017**, *226*, 10–17. [CrossRef]
37. Kitamura, M.; Ohkubo, I.; Matsunami, M.; Horiba, K.; Kumigashira, H.; Matsumoto, Y.; Koinuma, H.; Oshima, M. Electronic structure characterization of La_2NiMnO_6 epitaxial thin films using synchrotron-radiation photoelectron spectroscopy and optical spectroscopy. *Appl. Phys. Lett.* **2009**, *94*, 262503. [CrossRef]
38. Chanda, S.; Saha, S.; Dutta, A.; Sinha, T.P. Structural and transport properties of double perovskite Dy_2NiMnO_6. *Mater. Res. Bull.* **2015**, *62*, 153–160. [CrossRef]
39. Lan, C.; Zhao, S.; Xu, T.; Ma, J.; Hayase, S.; Ma, T. Investigation on structures, band gaps, and electronic structures of lead free La_2NiMnO_6 double perovskite materials for potential application of solar cell. *J. Alloys Compd.* **2016**, *655*, 208–214. [CrossRef]
40. Winkler, A.; Narayanan, N.; Mikhailova, D.; Bramnik, K.G.; Ehrenberg, H.; Fuess, H.; Vaitheeswaran, G.; Kanchana, V.; Wilhelm, F.; Rogalev, A.; et al. Magnetism in Re-based ferrimagnetic double perovskites. *New J. Phys.* **2009**, *11*, 073047. [CrossRef]
41. Majewski, P.; Geprägs, S.; Sanganas, O.; Opel, M.; Gross, R.; Wilhelm, F.; Rogalev, A.; Alff, L. X-ray magnetic circular dichroism study of Re 5d magnetism in Sr_2CrReO_6. *Appl. Phys. Lett.* **2005**, *87*, 202503. [CrossRef]
42. Leinenweber, K.; Parise, J.B. Rietveld refinement of Ca_2TiSiO_6 perovskite. *Am. Mineral.* **1997**, *82*, 475–478. [CrossRef]
43. Husain, M.; Rahman, N.; Azzouz-Rached, A.; Tirth, V.; Ullah, H.; Elhadi, M.; Uzair, M.; Alotaibi, A.; Humayun, Q.; Sfina, N.; et al. Exploring Silicon-Based Ca_2TiSiO_6 Ordered Double Perovskite Oxides: A Comprehensive DFT Investigation of Structural, Dynamical, Mechanical Stability, and Optoelectronic Properties. *Silicon* **2024**, *16*, 2781–2790. [CrossRef]
44. Du, X.; He, D.; Mei, H.; Zhong, Y.; Cheng, N. Insights on electronic structures, elastic features and optical properties of mixed-valence double perovskites $Cs_2Au_2X_6$ (X = F, Cl, Br, I). *Phys. Lett. A* **2020**, *384*, 126169. [CrossRef]
45. Sholagberu, A.A.; Yahya, W.A.; Adewale, A.A. Pressure effects on the opto-electronic and mechanical properties of the double perovskite $Cs_2AgInCl_6$. *Phys. Scr.* **2022**, *97*, 085824. [CrossRef]
46. Akter, H.; Hossain, M.M.; Uddin, M.M.; Naqib, S.H.; Ali, M.A. Effects of S substitution on the structural, optoelectronic, and thermomechanical properties of $KTaO_3$ through density functional theory. *J. Phys. Chem. Solids* **2024**, *190*, 112021. [CrossRef]
47. Dar, S.A.; Srivastava, V.; Sakalle, U.K.; Parey, V. Electronic structure, magnetic, mechanical and thermo-physical behavior of double perovskite Ba_2MgOsO_6. *Eur. Phys. J. Plus* **2018**, *133*, 64. [CrossRef]
48. Reuss, A. Berechnung der Fließgrenze von Mischkristallen auf Grund der Plastizitätsbedingung für Einkristalle. *ZAMM—J. Appl. Math. Mech./Z. Angew. Math. Mech.* **1929**, *9*, 49–58. [CrossRef]
49. Hill, R. The Elastic Behaviour of a Crystalline Aggregate. *Proc. Phys. Soc. Sect. A* **1952**, *65*, 349. [CrossRef]
50. Chung, D.H.; Buessem, W.R. The Voigt-Reuss-Hill (VRH) Approximation and the Elastic Moduli of Polycrystalline ZnO, TiO_2 (Rutile), and α-Al_2O_3. *J. Appl. Phys.* **1968**, *39*, 2777–2782. [CrossRef]
51. Audu, A.; Yahya, W.; Abdulkareem, A. Ab initio Studies of the Structural, Electronic and Mechanical Properties of $Zn_{1-x}Cr_xTe$. *J. Theor. Appl. Phys.* **2021**, *3*, 38.
52. Szeleszczuk, Ł.; Mądra-Gackowska, K.; Gackowski, M. Optoelectronic and thermoelectric performance of cubic X_2YInO_6 (X = Ba, Sr; Y = Nb, V) double perovskites: A first-principles approach. *Phys. B Condens. Matter* **2025**, *719*, 417958. [CrossRef]
53. Adewale, A.A.; Chik, A.; Adam, T.; Yusuff, O.K.; Ayinde, S.A.; Sanusi, Y.K. First principles calculations of structural, electronic, mechanical and thermoelectric properties of cubic $ATiO_3$ (A = Be, Mg, Ca, Sr and Ba) perovskite oxide. *Comput. Condens. Matter* **2021**, *28*, e00562. [CrossRef]
54. Qing, W.; Peng, J.; Wang, X. First principles investigation of pressure dependent stability, phonon, Debye temperature, physical, mechanical and thermodynamic properties of Rh3Al intermetallic compound. *Mol. Simul.* **2018**, *44*, 1554–1563. [CrossRef]
55. Anderson, O.L. A simplified method for calculating the debye temperature from elastic constants. *J. Phys. Chem. Solids* **1963**, *24*, 909–917. [CrossRef]
56. Tian, J.; Zhao, Y.; Hou, H.; Wang, B. The Effect of Alloying Elements on the Structural Stability, Mechanical Properties, and Debye Temperature of Al_3Li: A First-Principles Study. *Materials* **2018**, *11*, 1471. [CrossRef]
57. Marathe, M.; Grünebohm, A.; Nishimatsu, T.; Entel, P.; Ederer, C. First-principles-based calculation of the electrocaloric effect in $BaTiO_3$: A comparison of direct and indirect methods. *Phys. Rev. B* **2016**, *93*, 054110. [CrossRef]
58. Tariq, M.; Ali, M.A.; Laref, A.; Murtaza, G. Anion replacement effect on the physical properties of metal halide double perovskites Cs_2AgInX_6 (X = F, Cl, Br, I). *Solid State Commun.* **2020**, *314–315*, 113929. [CrossRef]

59. Yahya, W.; Yahaya, A.A.; Adewale, A.A.; Sholagberu, A.A.; Olasunkanmi, N.K. A DFT study of optoelectronic, elastic and thermo-electric properties of the double perovskites Rb_2SeX_6 (X = Br, Cl). *J. Niger. Soc. Phys. Sci.* **2023**, *5*, 1418. [CrossRef]
60. Huma, M.; Rashid, M.; Mahmood, Q.; Algrafy, E.; Kattan, N.A.; Laref, A.; Bhatti, A. Physical properties of lead-free double perovskites A_2SnI_6 (A = Cs, Rb) using ab-initio calculations for solar cell applications. *Mater. Sci. Semicond. Process.* **2021**, *121*, 105313. [CrossRef]
61. Zhao, S.; Lan, C.; Ma, J.; Pandey, S.S.; Hayase, S.; Ma, T. First principles study on the electronic and optical properties of B-site ordered double perovskite Sr_2MMoO_6 (M = Mg, Ca, and Zn). *Solid State Commun.* **2015**, *213–214*, 19–23. [CrossRef]
62. Hossain, A.; Ali, M.A.; Uddin, M.M.; Naqib, S.H.; Hossain, M.M. Theoretical studies on phase stability, electronic, optical, mechanical and thermal properties of chalcopyrite semiconductors $HgXN_2$ (X = Si, Ge and Sn): A comprehensive DFT analysis. *Mater. Sci. Semicond. Process.* **2024**, *172*, 108092. [CrossRef]
63. Shah, S.; Ali, Z.; Mehmood, S.; Khan, I.; Ahmad, I. Electronic structure, optical and magnetic properties of double Perovskites La_2MTiO_6 (M = Co, Ni, Cu and Zn). *Mater. Chem. Phys.* **2021**, *272*, 125050. [CrossRef]
64. Hossain, M.K.; Toki, G.F.I.; Samajdar, D.P.; Mushtaq, M.; Rubel, M.H.K.; Pandey, R.; Madan, J.; Mohammed, M.K.A.; Islam, R.; Rahman, F.; et al. Deep Insights into the Coupled Optoelectronic and Photovoltaic Analysis of Lead-Free $CsSnI_3$ Perovskite-Based Solar Cell Using DFT Calculations and SCAPS-1D Simulations. *ACS Omega* **2023**, *8*, 22466–22485. [CrossRef]
65. Carcione, J.M.; Cavallini, F.; Ba, J.; Cheng, W.; Qadrouh, A.N. On the Kramers-Kronig relations. *Rheol. Acta* **2019**, *58*, 21–28. [CrossRef]
66. Yang, B.-Y.; Zhang, J.-M.; Ali, A.; Huang, Y.-H.; Wei, X.-M. Computational investigation of structural, magnetic, electronic and optical properties of the cluster Mn-X_6 (X = P, S, Cl, Br or Te) doped monolayer WSe_2. *Thin Solid Film.* **2021**, *732*, 138793. [CrossRef]
67. Zarabinia, N.; Rasuli, R. Electronic and optical properties of halide double-perovskites under strain: A density functional study. *Energy Sources Part A Recovery Util. Environ. Eff.* **2021**, *43*, 2443–2455. [CrossRef]
68. Hossain, A.; Akhtaruzzaman, M.; Uddin, M.M. DFT-based design of X_3BiY_3 (X = Mg, Sr, Ba; Y = F, Cl) perovskites: From wide-gap insulators to promising semiconductors for solar cell applications. *J. Phys. Chem. Solids* **2026**, *208*, 113094. [CrossRef]
69. Abdulkadhim, T.M.J.; Alsaati Sa, A.; Shinen, M.H. Theoretical Investigation of Diameter Effects and Edge Configuration on the Optical Properties of Graphdiyne Nanotubes in the Presence of Electric Field. *J. Niger. Soc. Phys. Sci.* **2023**, *5*, 1083. [CrossRef]
70. Adewale, A.A.; Chik, A.; Yusuff, O.K.; Ayinde, S.A.; Sanusi, Y.K. First principle calculation of structural, electronic and optical properties of CdS and doped $Cd_{x-1}A_xS$ (A = Co, Fe, Ni) compounds. *Mater. Today Commun.* **2021**, *26*, 101882. [CrossRef]
71. Onuegbu, S.C.; Oluyamo, S.S.; Olusola, O.I. Influence of Bath pH values on the Structural and Optical Properties of Electrodeposited MgO Thin Films for Optoelectronic applications. *J. Niger. Soc. Phys. Sci.* **2023**, *5*, 931. [CrossRef]
72. Li, W.; Zhu, S.; Zhao, Y.; Qiu, Y. Structural, electrical, optical properties and stability of Cs_2InBr_5-yXy·H_2O (X = Cl, I, y = 0, 1, 2, 3, 4, 5) perovskites: The first principles investigation. *Thin Solid Film.* **2021**, *733*, 138805. [CrossRef]
73. Ali, M.H.; Islam, M.J.; Kumer, A.; Hossain, M.S.; Chakma, U.; Howlader, D.; Islam, T.; Hossain, T. Investigation of Structural, Electronic and Optical Properties of $Na_2InAgCl_6$, $K_2InAgCl_6$, and $Rb_2InAgCl_6$ Lead-Free Halide Double Perovskites Regarding with Cs2InAgCl6 Perovskites Cell and a Comparative Study by DFT Functionals. *Mater. Res.* **2021**, *24*, e20210086. [CrossRef]
74. Umm-e-Hani Murtaza, G.; Raza, H.H. Optoelectronic and thermal properties of cubic $SiMO_3$ (M = Sn, Pb) oxides for device application: A first principle study. *Opt. Quantum Electron.* **2020**, *52*, 456. [CrossRef]
75. Adewale, A.A.; Chik, A.; Adam, T.; Joshua, T.M.; Durowoju, M.O. Optoelectronic behavior of ZnS compound and its alloy: A first principle approach. *Mater. Today Commun.* **2021**, *27*, 102077. [CrossRef]
76. Giannozzi, P.; Andreussi, O.; Brumme, T.; Bunau, O.; Buongiorno Nardelli, M.; Calandra, M.; Car, R.; Cavazzoni, C.; Ceresoli, D.; Cococcioni, M.; et al. Advanced capabilities for materials modelling with Quantum ESPRESSO. *J. Phys. Condens. Matter* **2017**, *29*, 465901. [CrossRef]
77. Giannozzi, P.; Baroni, S.; Bonini, N.; Calandra, M.; Car, R.; Cavazzoni, C.; Ceresoli, D.; Chiarotti, G.L.; Cococcioni, M.; Dabo, I.; et al. QUANTUM ESPRESSO: A modular and open-source software project for quantum simulations of materials. *J. Phys. Condens. Matter* **2009**, *21*, 395502. [CrossRef]
78. Perdew, J.P.; Burke, K.; Ernzerhof, M. Generalized Gradient Approximation Made Simple. *Phys. Rev. Lett.* **1996**, *77*, 3865–3868. [CrossRef]
79. Heyd, J.; Scuseria, G.E.; Ernzerhof, M. Hybrid functionals based on a screened Coulomb potential. *J. Chem. Phys.* **2003**, *118*, 8207–8215. [CrossRef]
80. Nielsen, O.H.; Martin, R.M. First-Principles Calculation of Stress. *Phys. Rev. Lett.* **1983**, *50*, 697–700. [CrossRef]

Disclaimer/Publisher's Note: The statements, opinions and data contained in all publications are solely those of the individual author(s) and contributor(s) and not of MDPI and/or the editor(s). MDPI and/or the editor(s) disclaim responsibility for any injury to people or property resulting from any ideas, methods, instructions or products referred to in the content.